actuators

MDPI

Article

Closed-Loop Black-Box Identification of Active Magnetic Bearing System Under Decentralized Control

Penghui Zhang [1], Peng Wen [1], Yuexin Feng [2], Yuancheng Zhang [2], Jingchun Xu [2] and Zigang Deng [1,*]

[1] State Key Laboratory of Rail Transit Vehicle System, Southwest Jiaotong University, Chengdu 610031, China; zph@my.swjtu.edu.cn (P.Z.); 18328038991@163.com (P.W.)
[2] School of Information Science and Technology, Southwest Jiaotong University, Chengdu 611756, China; yc_zhang@my.swjtu.edu.cn (Y.Z.); xujingchun@my.swjtu.edu.cn (J.X.)
* Correspondence: deng@swjtu.cn

Abstract

Active magnetic bearings (AMBs) require accurate dynamic models for controller design and performance analysis, but their inherent open-loop instability makes modeling difficult under practical operating conditions. This study presents a closed-loop black-box identification method for an AMB system under decentralized control. A pseudo-random binary sequence (PRBS) excitation was injected into the closed-loop system, and the measured input–output data were used to estimate a nonparametric frequency-response model. The effects of excitation amplitude were first examined, and an excitation level of about 10–12% of the saturation current was found to provide a suitable balance among coherence, signal-to-noise ratio, and frequency-response variance. Based on the obtained frequency-domain data, ARX, output-error (OE), and state-space (SS) models were identified and compared. An initial model order range was estimated using the ARX structure and quantitative criteria, including the loss function and Bayesian information criterion. Within this candidate range, different model structures and orders were further evaluated. The 7th-order SS model showed the best overall agreement with the nonparametric frequency response and captured the dominant dynamic features more accurately. Independent time-domain validation and closed-loop reconstruction further confirmed that the selected SS model can represent the practical AMB dynamics with acceptable accuracy.

Keywords: active magnetic bearing; black-box identification; closed-loop identification; frequency-domain modeling

1. Introduction

Active magnetic bearings (AMBs) have attracted sustained interest for high-speed rotating machinery because they provide non-contact, oil-free rotor support with negligible mechanical wear and good adaptability to clean, hermetic, and other demanding operating environments [1,2]. These advantages make AMB systems attractive for turbomachinery, aerospace electric machines, flywheel systems, and high-speed spindles that require high precision and low friction [3,4]. In addition to active magnetic bearings, other magnetic suspension mechanisms have also been investigated. Passive magnetic bearings can reduce mechanical contact and power loss without continuous active control [5]. Hybrid passive magnetic-sliding bearings provide another practical solution for tunable axial equilibrium and wear reduction [6]. Active–passive supported rotor systems have also been studied for vibration suppression over a wide speed range, especially in flywheel applications [7].

Check for updates

Academic Editor: Guanghong Yang

Received: 6 May 2026
Revised: 18 June 2026
Accepted: 23 June 2026
Published: 4 July 2026

Copyright: © 2026 by the authors. Licensee MDPI, Basel, Switzerland. This article is an open access article distributed under the terms and conditions of the Creative Commons Attribution (CC BY) license.

These studies show that magnetic suspension systems may adopt different support mechanisms, but accurate dynamic models are still important for vibration analysis, controller design, and performance evaluation. Compared with passive or active–passive support systems, the present study focuses on the closed-loop identification of an active magnetic bearing system under decentralized control.

Because AMB systems are inherently open-loop unstable, feedback control is essential for stable operation. In recent years, a wide range of control strategies has been investigated for AMB systems, including PID control, fuzzy control, adaptive and robust control, sliding-mode control, and model predictive control [8,9]. Many advanced control methods, especially model predictive, robust, and LPV-based control schemes, rely on sufficiently accurate plant models for controller synthesis, stability analysis, and performance tuning [10,11]. Therefore, obtaining a reliable dynamic model of the controlled plant remains a key prerequisite for AMB controller design and practical implementation. System identification has become an effective way to obtain models directly from measured input–output data [12,13]. In engineering practice, model identification may become one of the most time-consuming stages in commissioning and controller development [14].

Existing system identification studies for AMB systems can be broadly classified into two categories, namely gray-box identification and black-box identification. In gray-box identification, the model structure is derived from physical knowledge of the system, while a limited set of uncertain parameters is estimated from measured data [15]. Cho et al. combined physical modeling and system identification for AMB systems and showed that first-principles models can be improved by experimental data [16]. Khader developed a commissioning-oriented identification framework in which the rigid-body dynamics were estimated by gray-box identification, while flexible modes were fitted separately from frequency-response data [17]. Yeh et al. proposed a closed-loop identification method for multi-axis AMB systems under decentralized and decoupling control using a gray-box structure [18]. These studies demonstrate that gray-box methods are effective when the physical structure of the AMB system is sufficiently clear.

Black-box identification does not require explicit physical equations of the plant and instead estimates a predefined model structure directly from experimental data. Therefore, black-box identification is often more flexible when the complete plant is difficult to describe analytically.

For this reason, black-box identification has attracted increasing interest in AMB research. Khader et al. used frequency-response data and prediction-error-based estimation to obtain linear black-box models for AMB commissioning [19]. Wallace et al. proposed a measurement-based black-box modeling approach for levitated AMB systems, in which frequency-domain data were used to construct a parametric model and reconstruct the closed-loop response [20]. Chiu developed a systematic identification procedure for the nonlinear closed-loop AMB system, where PAPRBS excitation was used, and different nonlinear models were compared for MIMO nonlinear dynamics [21]. These studies confirm that black-box identification can provide models that are directly useful for controller design and practical system analysis.

Despite these advances, several important gaps remain in the current AMB black-box identification literature. First, model order estimation, although critical to the accuracy–complexity trade-off, is often treated only briefly. Second, although different excitation signals have been analyzed and compared in AMB system identification, the effect of excitation amplitude on data quality and identification reliability has not been systematically clarified [22,23]. Third, existing studies often focus on frequency-domain fitting alone, whereas a more complete assessment combining frequency-domain agreement, independent time-domain validation, and closed-loop response reconstruction is still limited.

These gaps motivate the present study, in which a closed-loop black-box identification procedure is developed for an AMB system, and representative ARX, OE, and state-space models are utilized to fit the frequency-domain data. Further, the identified model is validated by independent data and closed-loop reconstruction. Based on the general system identification procedure of AMB systems, this paper aims to provide an experimentally verified closed-loop black-box identification procedure for an open-loop unstable AMB system under decentralized control. The main value of the work lies in the integration of excitation-amplitude evaluation, nonparametric frequency-response estimation, parametric model-order assessment, and closed-loop reconstruction verification.

The main contributions of this work are summarized as follows:

1. A closed-loop black-box identification workflow is established for the AMB system, covering excitation design, nonparametric frequency-response estimation, parametric model comparison, and closed-loop verification;
2. The influence of excitation amplitude is quantitatively analyzed using coherence, output-side signal-to-noise ratio, and frequency response variance, and a suitable excitation range is identified for the present system;
3. Three representative closed-loop identification approaches are summarized, and the plant frequency response is obtained using the indirect method and spectral analysis;
4. ARX, OE, and SS models are compared under the same frequency-domain framework, and the final model is selected based on frequency-domain fitting, time-domain prediction, and closed-loop reconstruction.

This paper is organized as follows. Section 2 introduces the AMB system configuration and presents the closed-loop identification methodology. Section 3 describes the proposed black-box identification procedure, including excitation signal selection, nonparametric frequency-domain model estimation, candidate model structures, model order estimation, and parameter estimation. Section 4 presents the identification results and model validation, including frequency-domain fitting, time-domain validation, and closed-loop reconstruction results. Finally, Section 5 summarizes the main conclusions of this study.

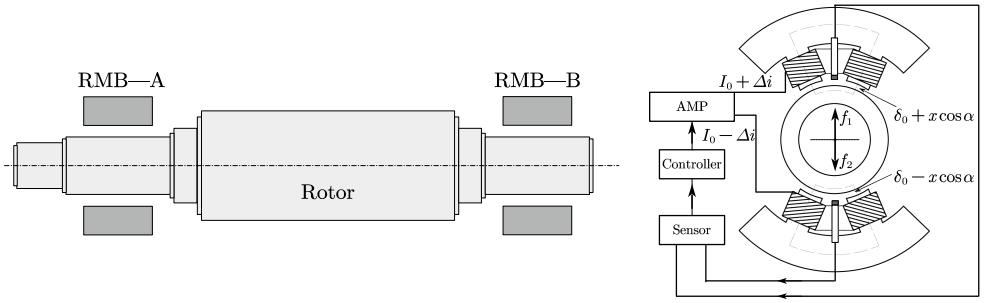
2. AMB System and Closed-Loop Identification Methodology

2.1. AMB System Configuration

Figure 1a shows the general configuration of the radial AMB system. The system mainly consists of a rotor and two radial magnetic bearings (RMB-A and RMB-B) located at different axial positions to provide non-contact radial support and stabilize the rotor around its equilibrium position. Each radial magnetic bearing regulates rotor motion in two mutually orthogonal radial directions (x and y control directions), resulting in a total of four control channels. In essence, the AMB system is a four-input four-output (4×4) MIMO (Multi-Input Multi-Output) system due to the inherent coupling among the channels. Nevertheless, with the decentralized control scheme employed in this work, the coupled multivariable system can be decomposed into four independent SISO (Single-Input Single-Output) subsystems, thereby simplifying both controller design and identification.

To verify the validity of the SISO treatment, each input channel (Ax, Ay, Bx, and By) was excited individually, and the responses of all four displacement channels were measured. The resulting 4×4 frequency responses are shown in Figure A1 in the Appendix A, based on the frequency-domain estimation method introduced later in Section 2.2. The residual coupling was quantified by the relative frequency-response level between each cross-channel response and the corresponding direct-channel response. A level of -20 dB was used as an engineering reference for weak coupling, corresponding to a cross-channel amplitude approximately one tenth of the direct-channel amplitude. Figure A1 shows that many off-diagonal responses are below this reference level over a large part of the

identification frequency range, while local residual coupling remains near several resonance regions. Thus, the four channels are approximately treated as weakly coupled SISO subsystems for the present control-oriented closed-loop identification.



(**a**) (**b**)

Figure 1. Schematic diagram of the active magnetic bearing system: (**a**) Configuration of AMB rotor system; (**b**) operating principle of single control loop.

The operating principle of a single radial magnetic bearing channel is illustrated in Figure 1b. During operation, the rotor displacement is measured by the position sensors and fed back to the controller. A bias current I_0 is applied to establish the nominal operating point, and a differential control current Δi is superimposed to generate the control force. Based on the measured displacement and the prescribed control law, the controller generates the control signal, which is amplified by the power amplifier and applied to the electromagnet coils. When the rotor deviates from its equilibrium position by a displacement x, the air gaps of the opposite poles vary accordingly, leading to unequal electromagnetic forces and hence a net restoring force. Through continuous adjustment of the control current, the rotor is stabilized around the desired equilibrium position. The nonlinear electromagnetic force F on the rotor is presented as:

$$F = \frac{\mu_0 N^2 A \cos\alpha}{4}\left(\frac{(I_0+\Delta i)^2}{(\delta_0+\Delta x\cos\alpha)^2} - \frac{(I_0-\Delta i)^2}{(\delta_0-\Delta x\cos\alpha)^2}\right) \tag{1}$$

where μ_0 is the permeability of air; N is the number of coil turns in a single pole; A is the pole face area; α is the pole deflection angle; δ_0 is the nominal radial air gap; Δi and Δx denote the control current variation and the rotor displacement from the center position, respectively.

The nonlinear electromagnetic force can be linearized around the equilibrium point (δ_0, I_0) as:

$$F_{\text{mag}} = k_i \Delta i + k_x \Delta x \tag{2}$$

where $k_x = -(\mu_0 N^2 A {I_0}^2 \cos^2\alpha)/\delta_0^3$ is the negative displacement stiffness; $k_i = (\mu_0 N^2 A I_0 \cos\alpha)/\delta_0^2$ is the current stiffness. More detailed descriptions of magnetic bearing systems can be found in [24].

Although a first-principles plant model combining Equation (2) could provide more physical interpretation, it requires detailed structural and electromagnetic parameters, such as the magnetic pole area, coil turns, bias current, air gap, actuator geometry, sensor dynamics, and amplifier characteristics. In the present experimental platform, these parameters are difficult to obtain accurately due to limited access to the internal design information of the AMB system. Therefore, a black-box identification approach is adopted in this study.

2.2. Closed-Loop Identification Approaches of SISO AMB System

Figure 2 shows the signal flow of one SISO control channel of the AMB system. An excitation signal u is added at the plant input for identification. The symbol $i_c = I_0 + \Delta I$ is the current command. The output of the plant is the rotor response, which is measured by the sensor and fed back to close the loop. In addition, disturbance d acts on the rotor, and measurement noise n is included in the feedback path. In this study, the identified object is defined as the plant model P from the injected current command to the measured rotor displacement. It includes the power amplifier, current loop, magnetic actuator, rotor dynamics, displacement sensor, and possible implementation delays. Therefore, the identified model should not be interpreted as a pure mechanical rotor model or a standalone electromagnetic actuator model [25].

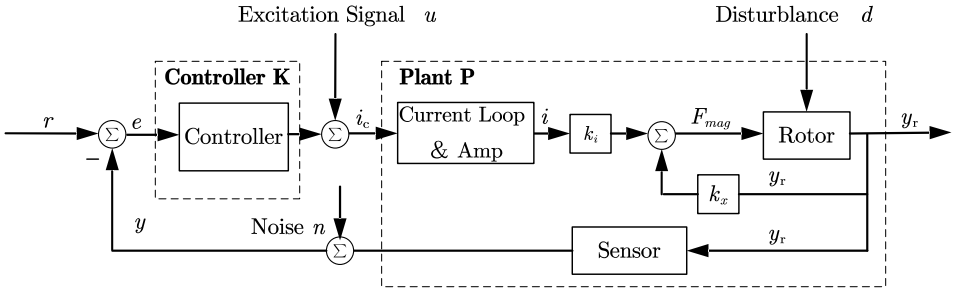


Figure 2. Block diagram of the SISO AMB control system and the related signal flow.

Owing to the inherent open-loop instability of the AMB system, closed-loop operation is required in the identification procedure. Let i_c denote the plant input and y the measured output. According to the signal flow in Figure 2, the system from $u(k)$ to $y(k)$ can be written as:

$$y(k) = \frac{P(q)}{1 + K(q)P(q)}u(k) + \frac{1}{1 + K(q)P(q)}n(k) \tag{3}$$

Based on this signal relation, three common closed-loop identification methods can be used in AMB systems [26,27].

1. Direct method;

In the direct method, the measured plant input i_c and output y are used directly to estimate the plant model:

$$y(k) = P(q)i_c(k) + n(k) \tag{4}$$

The direct method is easy to apply because the plant model is estimated directly from the measured plant input and output. Nevertheless, the correlation between the closed-loop input and the noise may introduce estimation bias.

2. Indirect method;

In the indirect method, the closed-loop transfer function from the excitation input u to the measured output y is identified first:

$$G_{yu}(q) = \frac{Y(q)}{U(q)} = \frac{P(q)}{1 + K(q)P(q)} \tag{5}$$

Then, with the known controller $K(q)$, the plant model can be recovered as:

$$P(q) = \frac{G_{yu}(q)}{1 - K(q)G_{yu}(q)} \tag{6}$$

The main advantage of the indirect method is that the excitation signal is independent of the measurement noise, which generally improves the reliability of the estimation.

3. Joint input–output method;

In the joint input–output method, both the plant input i_c and the measured output y are treated as outputs driven by the same excitation signal u:

$$\begin{aligned} G_{iu}(q) &= \frac{I_c(q)}{U(q)} = \frac{1}{1+K(q)P(q)} \\ G_{yu}(q) &= \frac{Y(q)}{U(q)} = \frac{P(q)}{1+K(q)P(q)} \end{aligned} \tag{7}$$

Therefore, the plant model can be obtained from the ratio of the two identified closed-loop transfer functions: $P(q) = G_{yu}(q)/G_{iu}(q)$. This method makes use of both the plant input and output signals and can provide richer information, but the identification procedure is more involved since two transfer functions must be estimated.

In this study, the indirect method is adopted because the controller used during the identification experiments is known and remains unchanged throughout the tests. It allows the plant model to be recovered from the identified closed-loop transfer function. The indirect identification method used in this study is based on the standard negative-feedback structure shown in Figure 2. The controller K(q) denotes the discrete-time PID (Proportional-Integral-Derivative) controller implemented in the dSPACE platform. During the following identification experiments, the controller parameters were kept unchanged for all excitation-amplitude tests. Moreover, the same sampling period is kept unchanged. The delays introduced by digital computation, ADC/DAC conversion, amplifier dynamics, current loop, actuator response, and sensor path are not separated explicitly. Instead, their effects are included in the plant model.

3. Black-Box Identification of AMB: A Procedure

3.1. Excitation Signal Selection

A suitable excitation signal is important for system identification. In engineering practice, broadband excitation signals are preferred because they can excite the system over a wide frequency range in a single test and thus improve identification efficiency. Common broadband excitation signals include chirp, white noise, PRBS, and multisine. Figure 3 compares the characteristics of these signals in discrete time-domain waveforms, the single-sided amplitude spectra, and the autocorrelation functions of these excitation signals.

As shown in Figure 3, different broadband excitation signals have different characteristics. White noise provides broadband excitation, but its randomness makes repeated experiments less consistent. The linear chirp signal is convenient for frequency-range inspection, while the multisine signal has clear spectral components and good periodicity, but only at selected frequencies. In contrast, the PRBS signal provides broadband and sufficiently strong excitation, while maintaining good repeatability and easy digital implementation. In addition, its autocorrelation is close to that of white noise, which makes it suitable for identifying the main dynamics of the AMB system. Therefore, the PRBS signal is selected in this study for closed-loop identification.

For a PRBS signal with order n, sampling interval T_s, repeated period number N_p, and the number of samples per bit N_b, the single period sequence length is $L = 2^n - 1$, the duration of a complete period is $T_{\mathrm{PRBS}} = N_p L N_b T_s$. The effective excitation frequency range can be approximately estimated from $f_{\min} = 1/(LN_bT_s)$ to $f_{\max} = 1/(2N_bT_s)$. The PRBS order, the number of samples per bit, and sequence length directly affect the estimated nonparametric frequency-response model results.

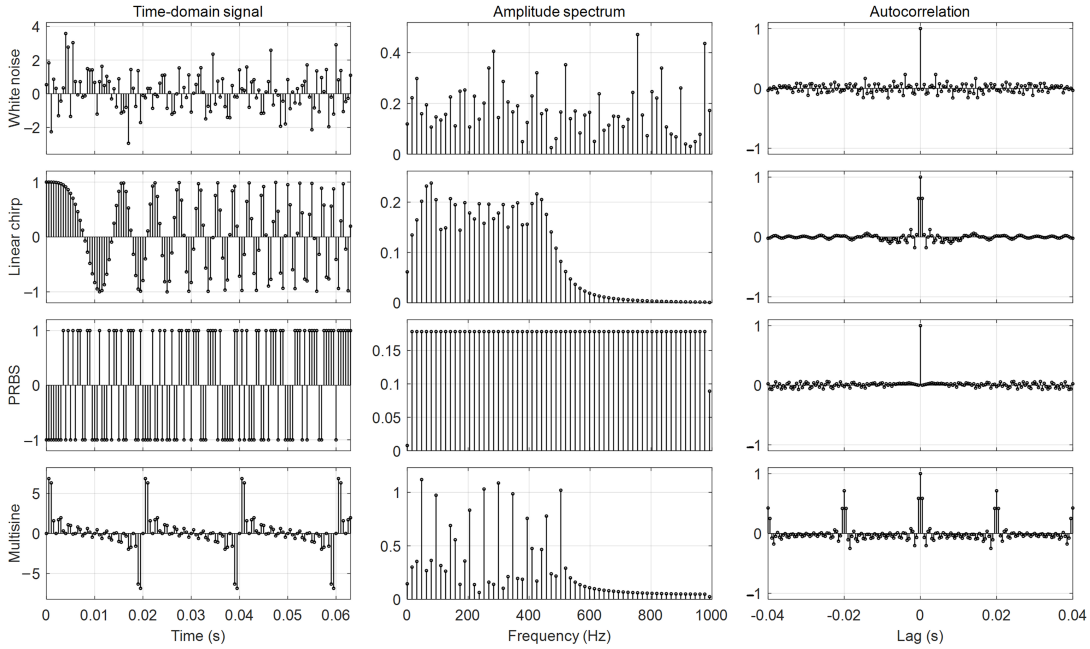
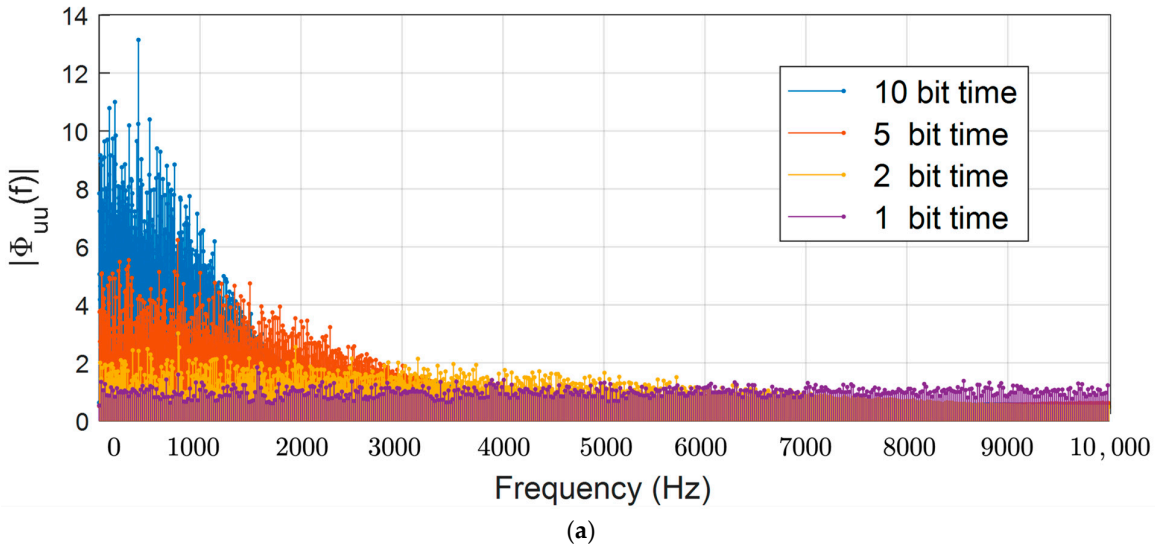


Figure 3. Comparison of broadband excitation signals for system identification in the time, frequency, and autocorrelation domains.

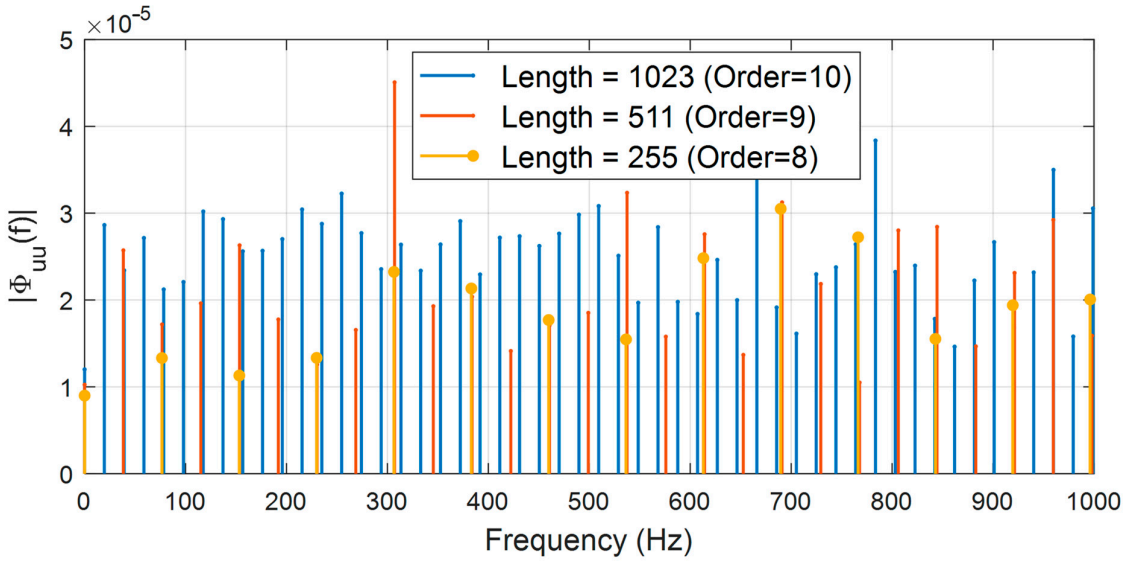
Figure 4 shows the influence of the PRBS bit time and sequence length on the excitation signal. As shown in Figure 4a, a larger bit time concentrates the excitation energy in the low-frequency range, whereas a smaller bit time extends the excitation bandwidth. Therefore, the bit time was selected according to the required identification frequency range. Figure 4b indicates that a longer PRBS sequence provides denser frequency components and improves the frequency resolution, but it also increases the experimental duration. In practice, the PRBS parameters need to be a compromise between excitation bandwidth, frequency resolution, and practical experimental time.

Another parameter that needs consideration is the amplitude of the excitation signal, and this will be discussed in the following part. After the PRBS excitation signal is designed, it is injected at the controller output of the closed-loop AMB system, and the excitation input u and the corresponding rotor response y are recorded synchronously.



(**a**)

Figure 4. *Cont.*



(**b**)

Figure 4. Influence of the PRBS parameters on the excitation signal characteristics: (**a**) influence of bit time; (**b**) influence of sequence length.

3.2. Nonparametric Model Estimation in the Frequency Domain

After data preprocessing, such as detrending, segmentation, and removal of abnormal samples, the frequency response from u to y can be estimated by nonparametric frequency-domain identification. Nonparametric frequency-response estimation methods mainly include the point-by-point frequency response method, the Fourier-transform-based method, and the spectral analysis method. In the point-by-point method, sinusoidal excitation is applied at each frequency of interest, and the steady-state response is measured. This method is intuitive but time-consuming. In the Fourier method, the input and output signals are transformed into the frequency domain, and the frequency response is estimated directly from their spectral ratio. This method is simple and efficient, but sensitive to noise. Spectral analysis reduces this sensitivity by using averaged auto- and cross-spectral estimates and thus provides better robustness against random noise. Therefore, for the PRBS excitation used in this study, the spectral analysis method is adopted to estimate the nonparametric frequency response.

Let $u(k)$ and $y(k)$ denote the sampled excitation input and output response, respectively. Their discrete Fourier transforms can be written as:

$$U(j\omega_k) = \sum_{n=0}^{N-1} u(n)e^{-j\omega_k n}, \quad Y(j\omega_k) = \sum_{n=0}^{N-1} y(n)e^{-j\omega_k n} \tag{8}$$

Based on the transformed data, the auto-spectrum of the input and the cross-spectrum between the input and output are defined as:

$$S_{uu}(j\omega_k) = \frac{1}{N}U(j\omega_k)U^*(j\omega_k), \quad S_{yu}(j\omega_k) = \frac{1}{N}Y(j\omega_k)U^*(j\omega_k) \tag{9}$$

where $(\cdot)^*$ denotes the complex conjugate. The nonparametric frequency response estimate from $u(k)$ to $y(k)$ is then obtained as:

$$\hat{G}_{yu}(j\omega_k) = \frac{S_{yu}(j\omega_k)}{S_{uu}(j\omega_k)} \tag{10}$$

The estimated nonparametric model in Equation (10) represents the transfer characteristic from the injected excitation u to the measured output y, and the frequency response of plant P can be derived from Equation (6) accordingly.

The injected excitation signal is generated independently of the noise measurement. Therefore, when the closed-loop transfer function is estimated using cross-spectral analysis, the influence of uncorrelated measurement noise on the mean estimate is reduced. During all excitation-amplitude tests, the controller configuration was unchanged, and the rotor displacement, control current, and amplifier saturation condition were monitored to confirm that the closed-loop system remained stable.

The excitation amplitude must be chosen with care, because its selection involves a trade-off between two conflicting requirements. A higher amplitude improves the signal-to-noise ratio and thus suppresses the relative effect of measurement noise, whereas a lower amplitude helps maintain the AMB system within its local linear operating region and reduces nonlinear distortion. Therefore, an appropriate excitation amplitude range is expected to exist. To evaluate the influence of excitation amplitude on the identified frequency-domain model, a series of excitation levels, expressed as percentages of the saturation current, was applied in the experiments. The resulting plant frequency responses up to 2100 Hz are shown in Figure 5.

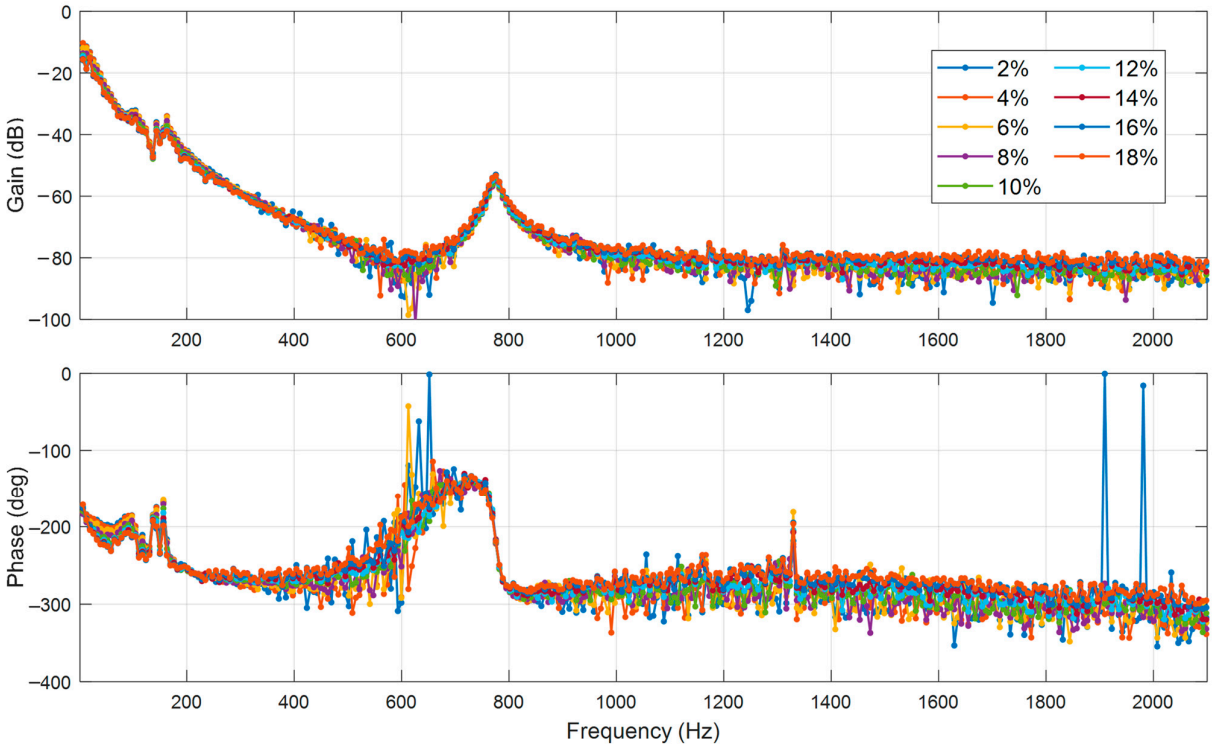


Figure 5. Identified nonparametric plant frequency responses under different excitation levels relative to the amplifier saturation current.

As shown in Figure 5, the nonparametric frequency-domain models identified under different excitation amplitudes exhibit generally consistent dynamic characteristics. The main resonance-related features around approximately 100 Hz, 150 Hz, and 780 Hz are captured in all cases.

Although the main dynamic features can be identified under different excitation amplitudes, the quality of the estimated frequency response still varies with the excitation level. Therefore, a quantitative comparison is further carried out using the average coherence, average FRF (frequency response function) variance, and output-side SNR, as shown

in Figure 6. The average coherence was obtained by averaging the magnitude-squared coherence, calculated from the auto- and cross-spectral densities of the excitation input and measured output, over the frequency range from 10 to 1000 Hz based on the coherence results. The FRF variance was estimated from repeated nonparametric frequency-response estimates obtained under multiple PRBS excitation periods. The output-side SNR was calculated as the ratio between the output power measured during PRBS excitation and the output noise power measured under the same closed-loop condition without external excitation. For each excitation amplitude, 50 repeated periods were conducted. Resonance regions were retained in the averaging because they contain important dynamic information of the AMB system. During the tests, the current command and amplifier output were monitored to ensure that actuator saturation did not occur. The maximum excitation amplitude was limited to 16% of the saturation current because the measured current approached the saturation limit when higher excitation amplitudes were applied.

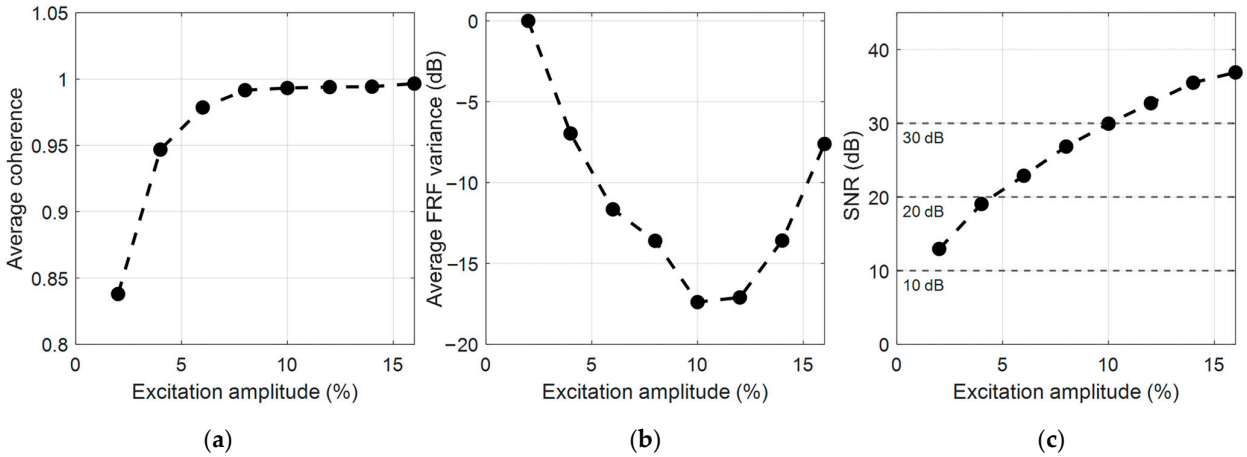


Figure 6. Quantitative comparison of identification quality under different excitation levels: (**a**) average coherence; (**b**) average FRF variance; (**c**) output-side SNR.

As shown in Figure 6a, the average coherence increases with excitation amplitude at first, but its growth becomes very small after about 8–10%, indicating that further increasing the amplitude contributes little to coherence improvement. In Figure 6b, the average FRF variance decreases first and then increases. This suggests that a small excitation amplitude is more affected by noise, while an excessively large amplitude may introduce stronger nonlinear effects and reduce the consistency of the identified model [28]. Figure 6c shows that the SNR increases as the excitation amplitude increases, which means that a larger amplitude helps improve the signal-to-noise ratio. Therefore, the excitation amplitude should be selected within a proper range rather than simply increased. For the present system, the results suggest that an amplitude of around 10–12% provides a good balance.

To further evaluate the influence of static operating-point variations, nonparametric frequency-response models were obtained under different bias currents and equilibrium air gaps. The nominal case, bias current variations of $\pm 20\%$, and equilibrium air-gap variations of ± 10 μm were compared, as shown in Figure 7. It can be observed that the frequency responses under different static operating conditions exhibit similar overall trends. The main dynamic characteristics, including the low-frequency response, the attenuation trend, and the resonance behavior, are generally consistent within the investigated frequency range. Some deviations appear near the resonance region and in the high-frequency range, indicating that the AMB dynamics are affected by the operating point. Therefore, the identified model should be regarded as a local linear representation around the tested operating condition. Nevertheless, the overall consistency of the frequency responses

suggests that the identified model has acceptable applicability within the investigated static operating range.

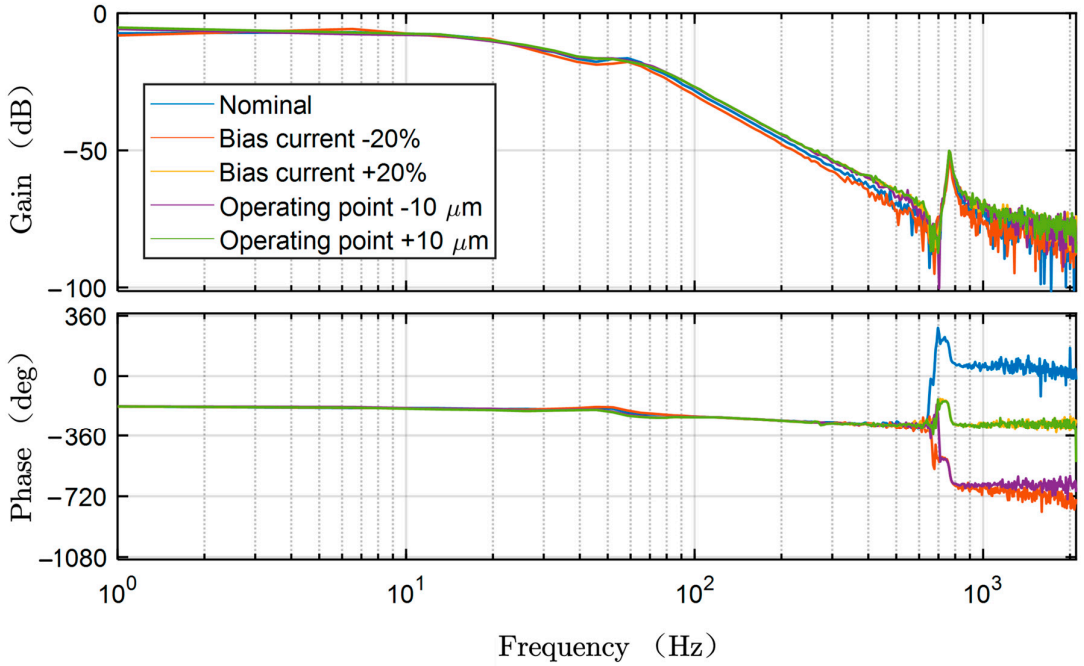


Figure 7. Comparison of nonparametric frequency-response models under different static operating conditions.

3.3. Candidate Black-Box Model Structures

Although black-box modeling does not require detailed prior knowledge of the internal physical mechanism, a suitable mathematical structure must still be chosen before parameter estimation. For linear time-invariant (LTI) systems, the black-box models considered in this study can be classified into two main categories: polynomial input–output models and state-space models.

3.3.1. Polynomial Input–Output Models

The polynomial input–output models describe the system directly by a difference equation between the input, output, and disturbance terms. A general form of the polynomial input–output model can be written as:

$$A(q^{-1})y(k) = \frac{B(q^{-1})}{F(q^{-1})}u(k - n_k) + \frac{C(q^{-1})}{D(q^{-1})}e(k) \tag{11}$$

where q^{-1} is the backward shift operator, $u(k)$ is the input, $y(k)$ is the output, $e(k)$ is the error term, and n_k is the input delay. The polynomials $A(q^{-1})$, $B(q^{-1})$, $C(q^{-1})$, $D(q^{-1})$, and $F(q^{-1})$ are used to describe the deterministic and stochastic parts of the system, with the orders n_a, n_b, n_c, n_d, and n_f, respectively. Different polynomial models are obtained by choosing different combinations of these polynomials, including:

- FIR model: $A(q^{-1}) = F(q^{-1}) = C(q^{-1}) = D(q^{-1}) = 1$; The FIR model only describes the input–output relation and does not include output feedback terms.
- ARX model: $F(q^{-1}) = C(q^{-1}) = D(q^{-1}) = 1$; The ARX model introduces an autoregressive output polynomial and has a simple structure with convenient parameter estimation.
- ARMAX model: $F(q^{-1}) = D(q^{-1}) = 1$; The ARMAX model further includes a moving-average disturbance term and is able to describe colored noise to some extent.

- OE model: $A(q^{-1}) = C(q^{-1}) = D(q^{-1}) = 1$; The OE model focuses on the system dynamics and is often suitable when the system transfer behavior is of primary interest.
- BJ model: $A(q^{-1}) = 1$; The BJ model uses separate polynomials for the plant and noise dynamics and therefore provides the most flexible description.

3.3.2. State-Space Model

In addition to the polynomial models, the state-space model represents the system dynamics in terms of state variables. Its general discrete-time form is given by:

$$\begin{aligned} x(k+1) &= Ax(k) + Bu(k) + w(k) \\ y(k) &= Cx(k) + Du(k) + e(k) \end{aligned} \tag{12}$$

where $x(k)$ is the state vector, and A, B, C, and D are the system matrices. $w(k)$ and $e(k)$ are state noise and measurement noise. Compared with polynomial input–output models, the state-space model provides a more compact description for high-order dynamics and is particularly useful when the system order is relatively high or when an extension to multivariable modeling is required.

For black-box identification of systems with unknown structures, it is generally necessary to test several candidate model structures and then determine the most suitable one based on the identification and validation results.

3.4. Model Order Estimation

Model order estimation is an important step in black-box identification. In practice, an inappropriate model order may lead to underfitting or overfitting and thus reduce the reliability of the identified model. A rough estimate of the system order can first be obtained from the identified nonparametric frequency-domain model. For a lightly damped system, one dominant resonance peak is often taken as an indication of one second-order mode. Therefore, the number of visible resonance peaks can provide an initial reference. It should be noted that this is only a preliminary estimate.

A more systematic order estimation can be carried out by analyzing the loss function V_N, which is expressed as:

$$V_N = \frac{1}{N}\sum_{k=1}^{N} \varepsilon^2(k) \tag{13}$$

where $\varepsilon(k)$ is the prediction error, N is the number of data samples.

In addition to the loss function, the Bayesian information criterion (BIC) introduces a penalty for overly high model orders and thus provides a compromise between accuracy and complexity. It is given by:

$$\mathrm{BIC} = N \ln(V_N) + n_\theta \ln N \tag{14}$$

where n_θ is the number of model parameters.

In this study, the ARX model is adopted for order estimation. The main reason is that the ARX structure is simple and suitable for rapid scanning over different candidate orders. Different sets of parameter combinations of n_a of $A(q^{-1})$ and n_b of $B(q^{-1})$ are calculated, and the results are shown in Figure 8.

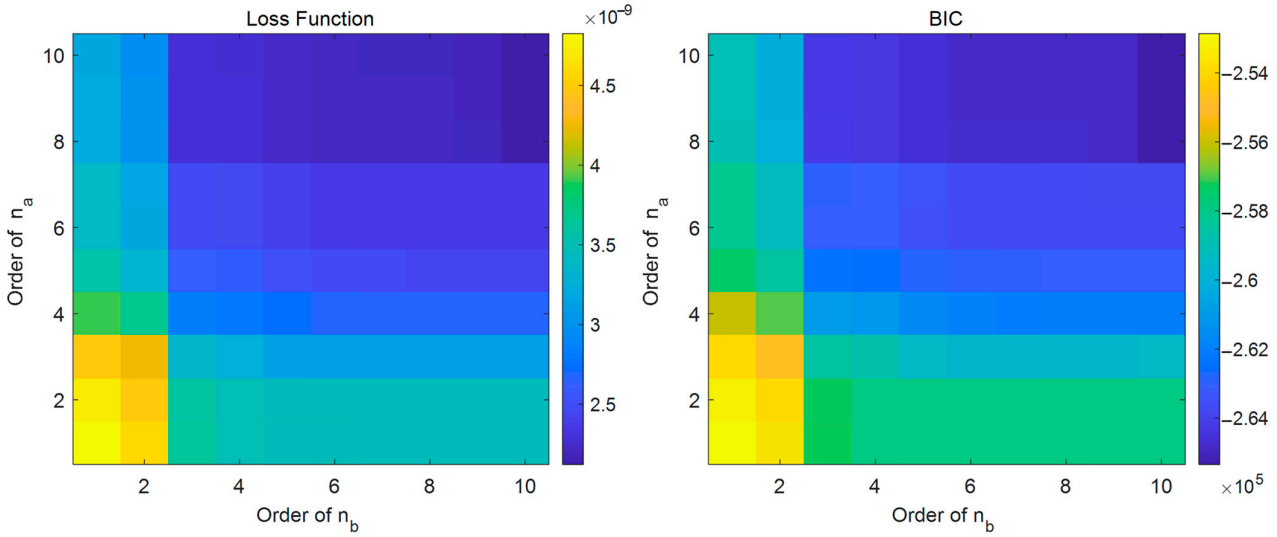


Figure 8. Heat maps of the loss function and BIC for different ARX orders.

It can be observed from the heat map that both indices decrease rapidly at low orders and then gradually level off as the order increases. This indicates that increasing the order improves the model fit at first, but the benefit becomes limited beyond a certain range. From the figure, a reasonable candidate order region can be identified around n_a = 5–9 and n_b = 4–6.

In addition, the plant model order can also be first estimated from the measured frequency response characteristics. In general, each dominant resonance peak is associated with a pair of complex-conjugate poles. Since three main resonance peaks (related to rigid and flexible rotor modes) can be observed in the identification frequency range, approximately six dynamic states are required to represent these dominant modes. Moreover, the identified assembled plant also includes the dynamics of the current loop, magnetic actuator, displacement sensor, and possible delays, which may introduce additional effective dynamics. Therefore, a model order of seven is a reasonable initial estimate.

3.5. Model Parameter Estimation

After a reasonable order range is obtained, the candidate models are estimated and compared. The order estimation gives a useful reference, but in practice, some trial-and-error adjustment is still needed to find the proper model.

For linear model structures of FIR and ARX, the parameter vector can be estimated by linear least squares. The general form to calculate the parameters is given by:

$$\hat{\theta}_{\mathrm{LS}} = (\Phi^{\mathrm{T}}\Phi)^{-1}\Phi^{\mathrm{T}}Y \tag{15}$$

where Y is the measured output vector, Φ is the regression matrix in Toeplitz form, and θ is the parameter vector to be estimated.

For model structures whose parameters enter the prediction nonlinearly, such as ARMAX, OE, and BJ, the parameters are usually estimated by nonlinear optimization, typically based on the prediction error method (PEM) [29], with the cost function of:

$$\hat{\theta}_{\mathrm{NL}} = \underset{\theta}{\operatorname{argmin}} \frac{1}{N}\sum_{k=1}^{N} \varepsilon^2(k,\theta) \tag{16}$$

The state-space model is usually estimated by a subspace method such as N4SID, and it can be further improved by the PEM method using subspace identification results as initial conditions. The principles of PEM and subspace methods can be found in [30].

Frequency-domain data are adopted in this study because they provide a clear description of resonance, bandwidth, and phase characteristics, and are widely used in engineering applications. Although several black-box model structures are available, only the OE, ARX, and SS models are considered in the following part, as they are supported for frequency-domain identification in MATLAB (2024b).

4. Results and Model Validation

In this section, system identification is carried out using the input PRBS excitation sequence $u(k)$ and the output rotor displacement signal $y(k)$. The PRBS signal is configured with $n = 10$, $T_s = 50$ us, $m = 20$, while each bit is maintained for five sampling points. Under these conditions, the frequency resolution is around 3.91 Hz, and the total excitation time is about 5.1 s. Figure 9 presents a segment of the measured input and output signals at an excitation level of 10% of the saturation current.

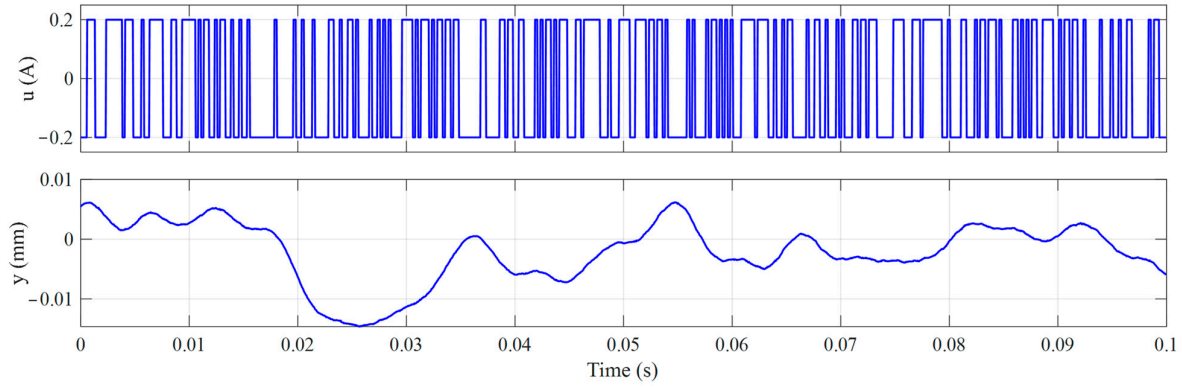


Figure 9. A segment of the measured PRBS input signal and output displacement signals.

4.1. Frequency Identification Results

Table 1 summarizes the identification performance of the ARX, OE, and SS models under different model orders. For the ARX model, the frequency-domain RMSE and time-domain fit vary considerably with the model order, and the overall validation performance remains relatively poor compared with the other two structures. The OE model gives more stable results, with a frequency-domain RMSE on the order of 10^{-4} and a time-domain fit above 76% for all tested orders. The SS model shows the best overall performance. In particular, the 7th-order SS model achieves nearly the lowest frequency-domain RMSE among the SS candidates, 4.969×10^{-4}, and also provides a high time-domain fit of 88.10%. Although the 9th-order SS model gives a slightly higher time-domain fit and frequency-domain RMSE value, the cost is the complexity of the model. Therefore, considering both frequency-domain accuracy and time-domain validation performance, the 7th-order model is selected for the subsequent comparison and validation.

Table 1. Identification performance of ARX, OE, and SS models under different model orders.

Model Structure	Evaluation Metric	5th-Order	6th-Order	7th-Order	8th-Order	9th-Order
ARX	Frequency-Domain RMSE	2.787×10^{-3}	3.183×10^{-3}	2.377×10^{-3}	3.070×10^{-3}	1.168×10^{-3}
	Time-Domain Fit (%)	33.23%	23.75%	43.06%	26.44%	50.25%
OE	Frequency-Domain RMSE	9.734×10^{-4}	7.785×10^{-4}	7.113×10^{-4}	9.650×10^{-4}	7.686×10^{-4}
	Time-Domain Fit (%)	76.68%	81.35%	82.96%	76.88%	81.58%
SS	Frequency-Domain RMSE	7.043×10^{-4}	7.971×10^{-4}	4.969×10^{-4}	7.253×10^{-4}	4.891×10^{-4}
	Time-Domain Fit (%)	83.13%	80.90%	88.10%	87.80%	88.16%

Selecting the model order solely according to the performance metrics in Table 1 may increase the risk of overfitting, especially for higher-order models. Therefore, the pole-zero maps of the 6th-, 7th-, 8th-, and 9th-order SS models were further examined, as shown in Figure 10. The higher-order models introduce additional pole-zero pairs, and some of them are located close to each other, indicating possible near pole-zero cancellations. These additional dynamics provide limited improvement to the dominant frequency-response characteristics but increase the model complexity. Therefore, the 7th-order SS model is selected as a reasonable compromise between fitting accuracy, dynamic representation, and model complexity.

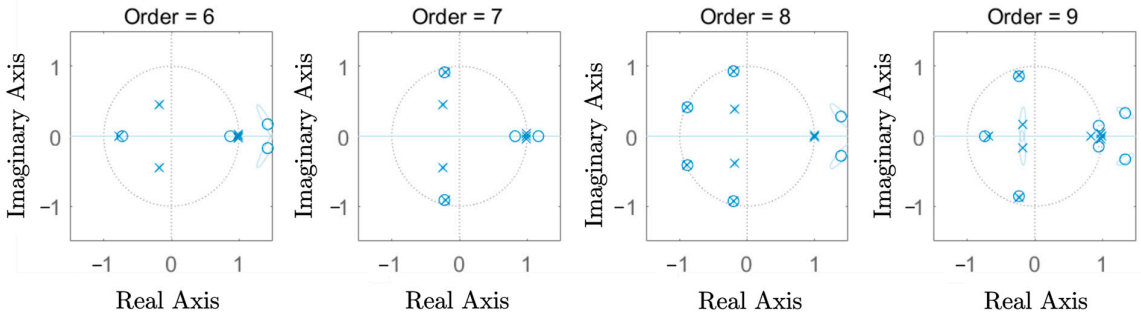


Figure 10. Pole-zero maps of the 6th-, 7th-, 8th-, and 9th-order SS models with confidence regions. The dotted circle denotes the unit circle. The symbols "×" and "○" represent poles and zeros, respectively.

Figure 11 compares the frequency-domain fitting results of the 7th-order OE, ARX, and SS models against the identified nonparametric frequency response up to 1000 Hz. It can be seen that the three models show different fitting characteristics over the frequency range of interest. The SS model gives the best overall agreement with the reference response and captures both dominant resonance peaks from 100 to 200 Hz. The OE model also follows the main trend of the measured response, but it only reproduces one of the two dominant resonance peaks, and its phase fit is less accurate in part of the middle-frequency range. In contrast, the ARX model provides a relatively accurate description in the high-frequency range, but it shows larger deviations below 200 Hz, especially around the main resonant dynamics. Therefore, among the three 7th-order models, the SS model provides the best frequency-domain fitting performance, followed by the OE model, while the ARX model is relatively less accurate.

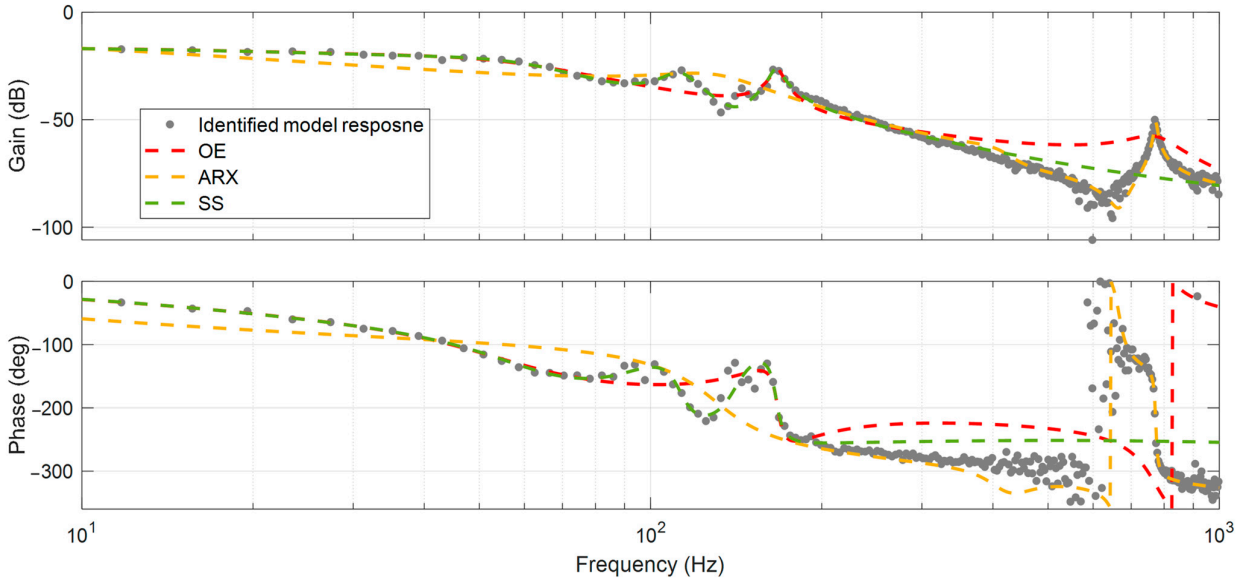


Figure 11. Frequency-domain fitting comparison of the 7th-order OE, ARX, and SS models with the nonparametric frequency response.

4.2. Model Validation

Although the frequency-domain fitting results reveal the differences among the candidate models, further validation in the time domain is still necessary. Therefore, an independent data set collected through identification is used to compare the measured and simulated responses of the OE, ARX, and SS models, and their comparisons are shown in Figure 12.

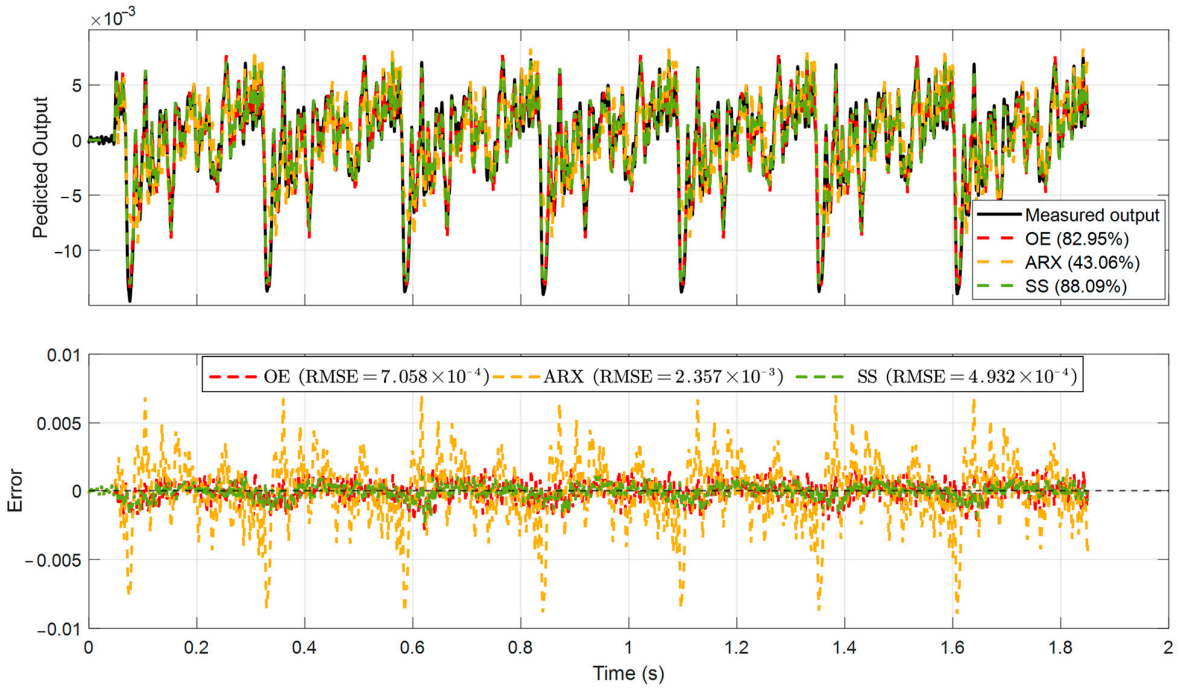


Figure 12. Time-domain validation results of the identified OE, ARX, and SS models: predicted output comparison and prediction error.

It can be observed that the SS and OE models show good agreement with the measured output and are able to reproduce the main response features, including the sharp periodic drops under periodic PRBS excitations. In contrast, the ARX model exhibits much larger

deviations and poorer tracking accuracy. This is also confirmed by the error curves, where the SS model gives the smallest error, followed by the OE model, while the ARX model shows the largest fluctuation. The quantitative results are consistent with this observation: the SS model achieves the highest fit and the lowest RMSE, the OE model gives slightly lower but still satisfactory accuracy, and the ARX model performs significantly worse. Based on the frequency-domain and time-domain comparison results, the 7th-order SS model is selected as the plant model.

To further assess the consistency between the identified model and the real AMB system under closed-loop operation, a chirp reference signal with an amplitude of 5 μm, a duration of 10 s, and a frequency range of 1–1000 Hz was applied to the experimental system, and the corresponding displacement and control current response were recorded. The closed-loop reconstruction is evaluated up to 1000 Hz because it covers the full operating range of the equipment with a margin. The purpose of this validation is to examine whether the identified assembled plant model can reproduce the dominant closed-loop response within the actual operating and control-relevant frequency range. Under the same excitation condition, the reconstructed closed-loop simulation based on the plant derived according to Equation (6) and the actual controller parameters was carried out. The comparison results are shown in Figure 13.

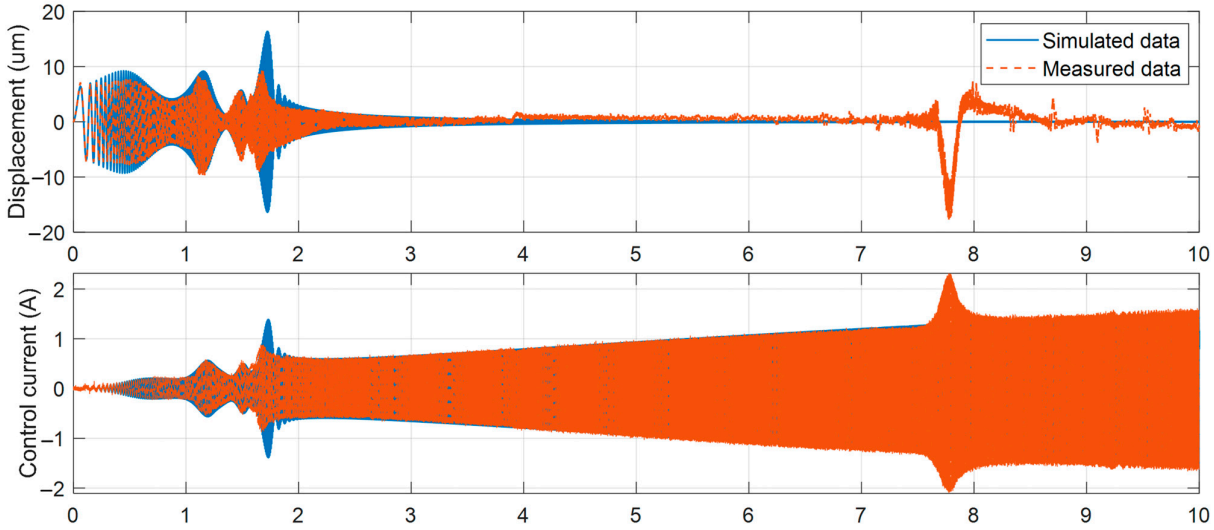


Figure 13. Comparison between the measured and simulated closed-loop responses under chirp reference excitation.

As shown in Figure 11, the simulated and measured responses exhibit good agreement in both displacement and control current before 7 s. The identified model captures the main oscillatory behavior, amplitude variation, and transient response in the resonance region with satisfactory accuracy. Some local discrepancies can still be observed, particularly near the resonance peak at approximately 1.6 s; nevertheless, the overall agreement indicates that the identified state-space model can effectively represent the closed-loop response within the validated operating frequency range.

A noticeable mismatch appears around 7.8 s in Figure 11. This discrepancy is mainly caused by the fact that the identified black-box model does not fully capture the first flexible mode around 780 Hz, as shown in Figure 9. Since this flexible mode is outside the normal operating frequency range of the platform, which mainly operates in the rigid-body mode, the mismatch has a limited influence on the intended application. Therefore, the independent validation results demonstrate that the identified state-space model can

represent the practical closed-loop AMB system with acceptable accuracy for rigid-body-mode operation.

To further verify the reliability of the identified model, Figure 14 shows the cross-correlation between the validation Chirp input and the model residual. Most correlation coefficients remain within the 95% confidence interval, although a few isolated points slightly exceed the interval due to the finite validation-data length. No continuous or systematic correlation pattern is observed. This result indicates that the residual is weakly correlated with the validation input, supporting the reliability of the identified model within the validated frequency range.

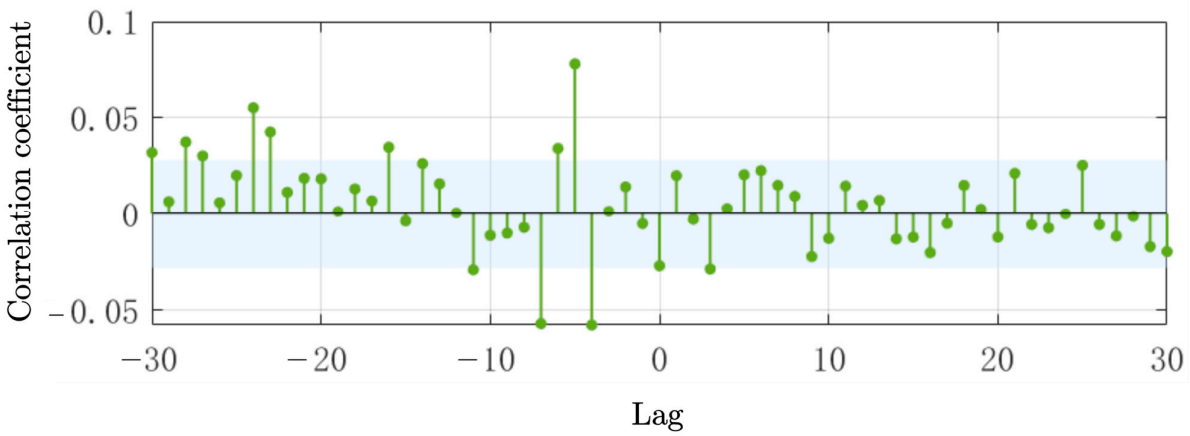


Figure 14. Cross-correlation between the validation input and the model residual. The shaded region denotes the 95% confidence interval.

It should be noted that the identified SS model is a nominal plant model under the present closed-loop operating condition. The controller parameters, bias current, and rotor equilibrium position were kept unchanged during the identification experiments. The model may change when the rotor speed or load varies. Therefore, the model under different operating conditions needs to be further identified and verified.

5. Conclusions

In this paper, a systematic workflow of a closed-loop black-box identification study was carried out for an AMB system, covering excitation design, frequency-domain modeling, parametric identification, and model validation. The main conclusions are as follows:

1. PRBS was chosen as the excitation signal because of its broadband excitation capability, good repeatability, and statistical properties similar to those of white noise. The excitation amplitude was also found to have a clear effect on identification quality. For the present AMB system and experimental conditions, an excitation amplitude of about 10–12% of the saturation current provides a suitable balance among coherence, SNR, and frequency response variance.
2. Model order estimation was carried out based on the information criteria of the loss function and the Bayesian information criterion. An initial candidate order range was obtained using the ARX model with the loss function and BIC. Within this range, different model structures and orders were further compared, and the 7th-order SS model was selected as a suitable trade-off between accuracy and complexity.
3. Three candidate model structures, namely ARX, OE, and SS models, were fitted to the frequency-domain data. The SS model gave the best overall fitting result, with the smallest frequency-domain RMSE and an accurate representation of the two dominant dynamic features. The OE model also produced a similar but less accurate result, while the ARX model showed relatively larger deviations.

4. Time-domain validation confirmed that the state-space model provided the best overall performance, while the ARX model showed the largest deviation, and the OE model gave intermediate results. The identified 7th-order state-space model was then combined with the actual controller parameters to reconstruct the closed-loop system. The good agreement between the simulated and measured closed-loop responses demonstrated that the selected model could represent the practical AMB dynamics with acceptable accuracy.

Future work will focus on two aspects. First, the present study will be extended to MIMO black-box identification, so that the cross-coupling dynamics of the AMB system can be described more fully. Second, further research will be carried out on data-driven identification and modeling methods to enhance model accuracy and engineering applicability.

Author Contributions: Conceptualization, P.Z. and Z.D.; methodology, P.Z. and Y.Z.; software, P.Z. and J.X.; validation, P.Z. and P.W.; formal analysis, Y.F. and P.Z.; investigation, P.Z. and Y.Z.; resources, Z.D.; data curation, P.Z.; writing—original draft preparation, P.Z.; writing—review and editing, P.Z., Y.F., and Z.D.; visualization, P.Z.; supervision, Z.D.; project administration, Z.D. All authors have read and agreed to the published version of the manuscript.

Funding: This work was partially supported by Shandong Provincial Technology Innovation Guidance Program (Central Government Fund for Guiding Local Science and Technology Development) under Grant YDZX2025076.

Institutional Review Board Statement: Not applicable.

Informed Consent Statement: Not applicable.

Data Availability Statement: The data presented in this study are available from the corresponding author upon reasonable request.

Conflicts of Interest: The authors declare no conflicts of interest.

Appendix A

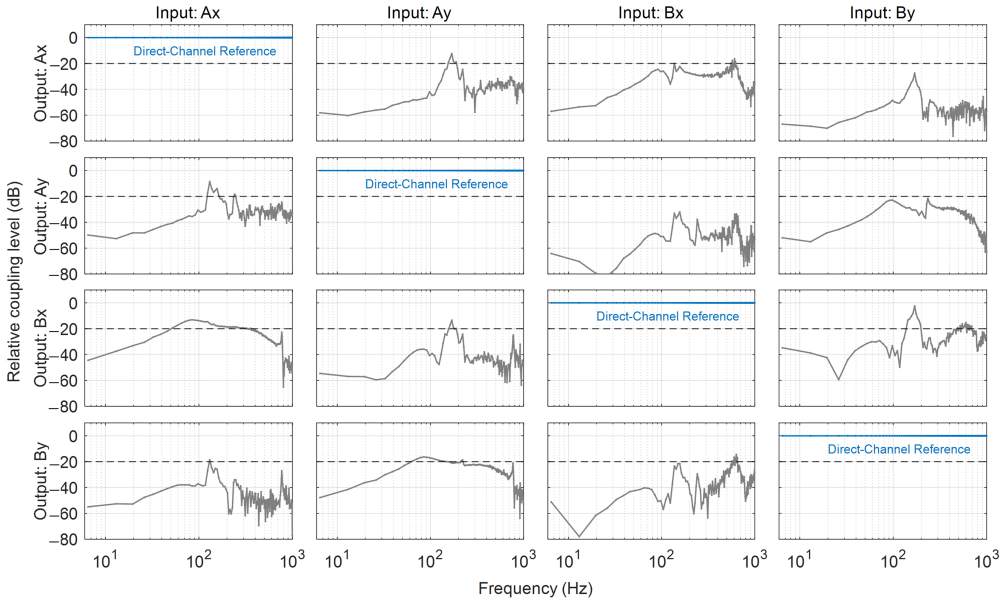


Figure A1. Relative coupling levels of the measured 4 × 4 frequency responses of the radial AMB system. The diagonal terms are set to 0 dB as the direct-channel references. The off-diagonal terms represent the cross-channel responses relative to the corresponding direct-channel responses. The dashed line at −20 dB is used as an engineering reference for weak coupling.

References

1. Breńkacz, Ł.; Witanowski, Ł.; Drosińska-Komor, M.; Szewczuk-Krypa, N. Research and applications of active bearings: A state-of-the-art review. *Mech. Syst. Signal Process.* **2021**, *151*, 107423. [CrossRef]
2. Du, Y.; Zhang, G.; Hua, W. Review on Research and Development of Magnetic Bearings. *Energies* **2025**, *18*, 3222. [CrossRef]
3. Karafi, M.R.; Asef, P. Review of Emerging Hybrid Gas–Magnetic Bearings for Aerospace Electrical Machines. *World Electr. Veh. J.* **2025**, *16*, 662. [CrossRef]
4. Xiong, W.; Sun, W.; Liu, K.; Xu, M.; Pei, T. Active Magnetic Bearing Technology Development in High-Speed Motorized Spindles. *J. Mech. Eng.* **2021**, *57*, 1–17. [CrossRef]
5. Vigliani, A.; Cavallaro, S.P.; Venturini, S. Modelling and Experimental Testing of Passive Magnetic Bearings for Power Loss Reduction. *Appl. Sci.* **2025**, *15*, 4149. [CrossRef]
6. Tanabi, N.; Cardoso, J.R.; Tsuzuki, M.S.G.; Maruyama, N.; Pavani, R.A.; Horikawa, O. Hybrid Passive Magnetic-Sliding Bearing with Tunable Axial Equilibrium: Design Guidelines and Experimental Wear Assessment. *IEEE Access* **2026**, *14*, 42119–42131. [CrossRef]
7. Hu, M.; Zeng, Y.; Li, D.; Luo, H.; Wei, J.; Liu, K. 4-DOF Full-Speed Range Vibration Suppression of an Active–Passive Supported Flywheel Rotor Based on Inverse System Decoupling. *Actuators* **2026**, *15*, 157. [CrossRef]
8. Kamath, K.P.; Bekinal, S.I.; Vijay, G.S.; Doddamani, M. Review of control strategies for active magnetic bearings. *Cogent Eng.* **2025**, *12*, 2467145. [CrossRef]
9. Morsi, A.; Abbas, H.S.; Ahmed, S.M.; Mohamed, A.M. Model predictive control based on linear parameter-varying models of active magnetic bearing systems. *IEEE Access* **2021**, *9*, 23633–23647. [CrossRef]
10. Xu, Y.; Wang, X.; Liu, M.; Li, N.; Yu, T. Adaptive robust control of active magnetic bearings rigid rotor systems. *J. Power Electron.* **2023**, *23*, 1004–1015. [CrossRef]
11. Li, L.; Gao, L.; Ou, M. Suppression of disturbances in closed-loop active magnetic bearing system with time-varying delay based on H_∞ state feedback control. *IEICE Trans. Electron.* **2025**, *E108-C*, 613–620. [CrossRef]
12. Wang, Z.; Wu, H.; Song, X.; Zou, Y.; Sa, X.; Zhao, Z. A review of system identification for active magnetic bearings: A closed-loop perspective from theory to engineering validation. *Int. J. Dyn. Control* **2026**, *14*, 67. [CrossRef]
13. Sun, Z.; He, Y.; Zhao, J.; Shi, Z.; Zhao, L.; Yu, S. Identification of active magnetic bearing system with a flexible rotor. *Mech. Syst. Signal Process.* **2014**, *49*, 302–316. [CrossRef]
14. Samad, T.; Bauer, M.; Bortoff, S.; Di Cairano, S.; Fagiano, L.; Odgaard, P.F.; Rhinehart, R.R.; Sánchez-Peña, R.; Serbezov, A.; Ankersen, F.; et al. Industry engagement with control research: Perspective and messages. *Annu. Rev. Control* **2020**, *49*, 1–14. [CrossRef]
15. Jiang, H.; Su, Z.; Wang, D.; Wu, C. Multiparameter identification for active magnetic bearing with uncertainties based on a coupled nonlinear model. *IEEE Trans. Ind. Electron.* **2023**, *70*, 10431–10441. [CrossRef]
16. Cho, Y.M.; Srinivasan, S.; Oh, J.-H.; Kim, H.S. Modelling and system identification of active magnetic bearing systems. *Math. Comput. Model. Dyn. Syst.* **2007**, *13*, 125–142. [CrossRef]
17. Khader, S.A. System Identification of Active Magnetic Bearing for Commissioning. Master's Thesis, Uppsala University, Uppsala, Sweden, 2015.
18. Yeh, T.-J.; Huang, C.-C.; Toh, C.-S. Closed-loop identification of multi-axis active magnetic bearing systems based on decentralized and decoupling control. *Mechatronics* **2023**, *90*, 102933. [CrossRef]
19. Khader, S.A.; Liu, B.; Sjöberg, J. System identification of active magnetic bearing for commissioning. In Proceedings of the 6th International Conference on Modelling, Identification and Control (ICMIC), Melbourne, Australia, 3–5 December 2014; pp. 289–294. [CrossRef]
20. Wallace, B.; Nesbitt, M.; Lee, J. Measurement-based dynamic modelling in levitated active magnetic bearing systems. *Int. J. Precis. Eng. Manuf.-Smart Technol.* **2024**, *2*, 169–177. [CrossRef]
21. Chiu, H.-L. Identification approach for nonlinear MIMO dynamics of closed-loop active magnetic bearing system. *Appl. Sci.* **2022**, *12*, 8556. [CrossRef]
22. Vuojolainen, J.; Nevaranta, N.; Jastrzebski, R.; Pyrhönen, O. Comparison of excitation signals in active magnetic bearing system identification. *Model. Identif. Control* **2017**, *38*, 123–133. [CrossRef]
23. Schietecat, M.; Jacobs, L.; Swevers, J. Nonparametric frequency-domain identification of magnetic bearings: An experimental study. *IFAC-PapersOnLine* **2024**, *58*, 103–108. [CrossRef]
24. Maslen, E.H.; Schweitzer, G. (Eds.) *Magnetic Bearings: Theory, Design, and Application to Rotating Machinery*; Springer: Berlin/Heidelberg, Germany, 2009. [CrossRef]
25. Xiong, F.; Yin, T.; Zhang, N.; Xu, W.; Li, Y. System Identification and Robust Control Method for Magnetic Bearings in Ship Propulsion Shaft Systems. *J. Mar. Sci. Eng.* **2025**, *13*, 2096. [CrossRef]
26. Pintelon, R.; Schoukens, J. *System Identification: A Frequency Domain Approach*, 2nd ed.; IEEE Press: Hoboken, NJ, USA, 2012. [CrossRef]

27. Doraiswami, R.; Diduch, C.; Stevenson, M. Closed loop identification. In *Identification of Physical Systems: Applications to Condition Monitoring, Fault Diagnosis, Soft Sensor and Controller Design*; John Wiley & Sons, Ltd.: Chichester, UK, 2014; pp. 357–378. [CrossRef]
28. Noël, J.-P.; Kerschen, G. Nonlinear system identification in structural dynamics: 10 more years of progress. *Mech. Syst. Signal Process.* **2017**, *83*, 2–35. [CrossRef]
29. Wang, J.; Ramirez-Mendoza, R.A. The practical analysis for closed-loop system identification. *Cogent Eng.* **2020**, *7*, 1796895. [CrossRef]
30. Ljung, L. *System Identification: Theory for the User*, 2nd ed.; Prentice Hall PTR: Upper Saddle River, NJ, USA, 1999.

Disclaimer/Publisher's Note: The statements, opinions and data contained in all publications are solely those of the individual author(s) and contributor(s) and not of MDPI and/or the editor(s). MDPI and/or the editor(s) disclaim responsibility for any injury to people or property resulting from any ideas, methods, instructions or products referred to in the content.